

Atomistic Simulation of Phonon and Magnon Thermal Transport across the Ferro-Paramagnetic Transition

Yanguang Zhou,¹ Julien Tranchida,^{2,*} Yijun Ge,¹ Jayathi Murthy,^{1,†} and Timothy S. Fisher^{1,‡}

¹*Mechanical and Aerospace Engineering Department,
University of California Los Angeles, Los Angeles, CA 90095, USA*

²*Multiscale Science Department, Sandia National Laboratories,
P.O. Box 5800, MS 1322, Albuquerque, NM 87185, USA*

(Dated: November 26, 2021)

A temperature-dependent approach involving Green-Kubo equilibrium atomic and spin dynamics (GKEASD) is reported to assess phonon and magnon thermal transport processes accounting for phonon-magnon interactions. Using body-center cubic (BCC) iron as a case study, GKEASD successfully reproduces its characteristic temperature-dependent spiral and lattice thermal conductivities. The non-electronic thermal conductivity, i.e., the summation of phonon and magnon thermal conductivities, calculated using GKEASD for BCC Fe agrees well with experimental measurements. Spectral energy analysis shows that high-frequency phonon-magnon scattering rates are one order magnitude larger than those at low frequencies due to energy scattering conserving rules and high density of states. Higher temperatures further accentuate this phenomenon. This new framework fills existing gaps in simulating thermal transport across the ferro- to para-magnetic transition. Future application of this methodology to phonon- and magnon-dominant insulators and semiconductors will enhance understanding of emerging thermoelectric, spin caloritronic and superconducting materials.

I. INTRODUCTION

A better understanding of heat transfer considering interactions among different temperature-induced excitations in crystals, e.g., phonons, electrons and spins, is of great importance in many disciplines, including thermoelectric [1–3], spin caloritronic [4] and superconducting materials [5]. Unlike phonons and electrons, whose thermal transport properties have been well studied, the heat transport behavior of magnons - collective excitations of magnetic spins - is poorly understood at the fundamental level. Little is known about the influence of phonon-magnon and magnon-magnon scattering on heat transfer. For example, the experimental lattice thermal conductivities of magnetic materials such as body-centered cubic (BCC) iron [6, 7], face-centered cubic (FCC) nickel [8], YMnO_3 , LuMnO_3 and ScMnO [9], as well as CrN [10, 11], show significantly different temperature dependences near the Curie temperature (T_c), compared to the typical $1/T$ relation at high temperatures when only phonons are considered [12–14]. The magnetic configuration changes from a ferromagnetic state at low temperature in which spins are aligned to a paramagnetic state above the Curie temperature in which the spin configuration is fully disordered [15].

To model the thermal transport properties of magnetic materials, temperature-dependent lattice and magnetic excitations must be taken into consideration when calculating the inputs, e.g., heat current or force constants, for thermal conductivity. To date, theoretical studies have sought to develop explanations for mutual interactions between phonons and magnons [15–19]. However, most such studies provide only a partial treatment based on thermodynamic properties [15, 20], average phonon-magnon relaxation times [16], and phonon-magnon temperature gradients [18]. A robust framework to compute thermal transport properties such as thermal conductiv-

ity and modal scattering rates in magnetic materials is still lacking.

In this paper, a temperature-dependent method - Green-Kubo equilibrium atomic and spin dynamics (GKEASD) - based on linear response theory [21] and spin-lattice dynamics (SLD) [22] is reported to calculate the thermal transport properties of phonons and magnons in magnetic materials. In GKEASD, phonon-phonon scattering (PPS), phonon-magnon scattering (PMS) and magnon-magnon scattering (MMS) are inherently included. As a proof of concept, our study focuses on a model system consisting of a simple transition-metal ferromagnet, BCC iron, with a Curie temperature of 1043 K. Using this methodology, we successfully reproduce the characteristic temperature-dependent non-electronic thermal conductivity observed in experiments for magnetic materials [6–10, 23]. Modal level phonon-phonon, magnon-magnon and phonon-magnon scattering rates are then quantified using spectral energy density (SED) analysis. The agreement between theoretical predictions and experimental measurements establishes the reliability of the methodology.

II. COMPUTATIONAL METHODS

A. Spin Lattice Dynamics

Here, a symplectic and scalable algorithm for spin lattice dynamic (SLD) that was recently developed [22] and embedded in the Large-scale Atomic/Molecular Massively Parallel Simulator (LAMMPS) [24] is applied to describe the atomic spins in magnetic crystals from the ferromagnetic limit to the paramagnetic limit (**Figure 1**). Compared to classical molecular dynamics (MD), this new algorithm augments the phase space by adding a classical spin vector \vec{s} to each magnetic atom i , in addition to its position \vec{r} and momentum \vec{p} . The motion

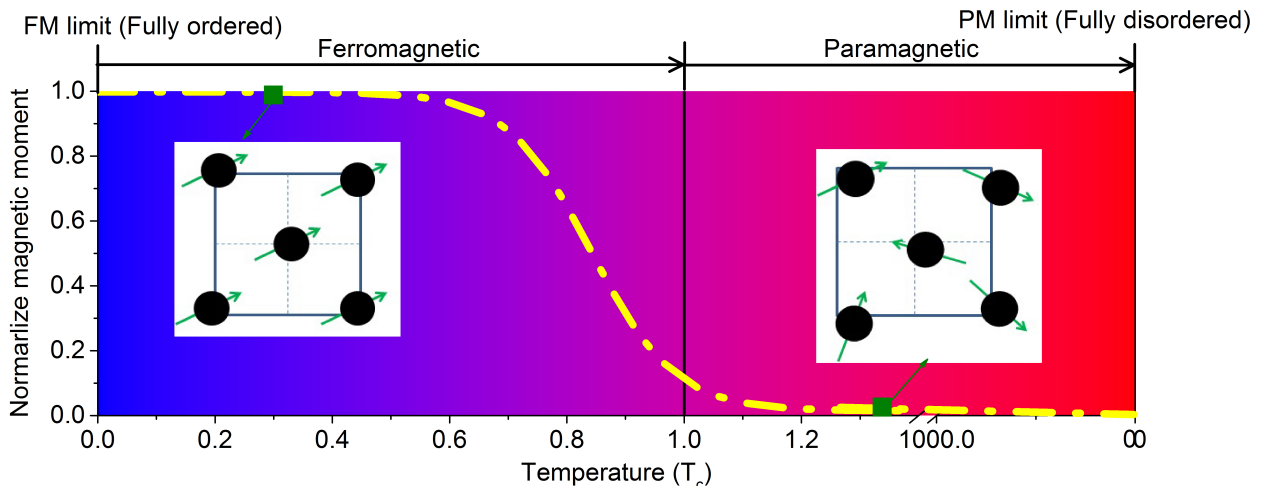


FIG. 1: Magnetic state of system vs. temperature. The arrows indicate the spin in the system.

equations of atoms and spins can be written as

$$\frac{d\vec{r}_i}{dt} = \frac{\vec{p}_i}{m_i} \quad (1)$$

$$\frac{d\vec{p}_i}{dt} = \sum_{i \neq j}^N \left[-\frac{dV(|\vec{r}_{ij}|)}{d|\vec{r}_{ij}|} + \frac{dJ(|\vec{r}_{ij}|)}{d|\vec{r}_{ij}|} \vec{s}_i \cdot \vec{s}_j \right] \vec{e}_{ij} \quad (2)$$

$$\frac{d\vec{s}_i}{dt} = \vec{f}_i \times \vec{s}_i \quad (3)$$

where \vec{e}_{ij} is the unit vector along \vec{r}_{ij} and \vec{f}_i is the analog of a spin force applied on the spin. Spin dynamics simulations without introducing the influence of the lattice, i.e., fixed atomic position, are implemented in a NVT ensemble (constant number of particles, volume and temperature) for 200 ps to reach the target temperature, and then a NVE ensemble (constant number of particles, volume and energy) is run for 200 ps to compute the heat flux associated with the spins.

For a system with lattice vibrations, a NVT simulation for 200 ps is first run to reach the target temperature. Then, a NVE ensemble for 200 ps is used to obtain the heat flux of the magnons. A time step of 0.2 fs is used in all simulations. The spin potential used in our study is fitted using first principles calculations. The magnon dispersion generated from this potential fits experiments well (details can be found in [22]). Mechanical interactions among atoms are computed using the embedded-atom method (EAM) potential [25, 26]. To assess the accuracy of the potential, we compare the phonon dispersion (**Appendix A**) as well as lattice thermal conductivity from MD and *ab initio* calculations, good agreement is found.

B. First Principles Calculations

In this paper, all first-principles simulations are implemented via Vienna Ab-initio Simulation Package (VASP) based on density functional theory (DFT). The pseudopotential with a generalized gradient approximation (GGA) parameterized by Perdew-Burke-Ernzerhof

(PBE) theory [27] for the exchange-correlation functional is used to depict the system. Periodic boundary conditions are applied in the three directions. A plane basis with a cutoff energy of 520 eV is used in all simulations. The Monkhorst-Pack scheme is used to generate $2 \times 2 \times 2$ k-point mesh for the primitive cell and $6 \times 6 \times 6$ supercell. Before performing electrostatic potential or interatomic force constant calculations, the atomic structure and cell size are fully relaxed until the energy difference and the Hellman-Feynman force converges to within 1×10^{-6} eV and 1×10^{-5} eV/Å, respectively. The $6 \times 6 \times 6$ supercell with an energy criterion of 1×10^{-6} eV in the self consistent calculation is used to extract 2nd and 3rd force constants.

C. Green-Kubo Equilibrium Atomic and Spin Dynamic Simulations

During MD simulations for lattice thermal conductivity calculations, we first run the NVT ensemble for 200 ps with a time step of 0.2 fs to make the lattice and spin attain the target temperature. Then a canonical ensemble is run for the next 400 ps to generate heat current, which is the input for the calculation of the lattice thermal conductivity using Green-Kubo equilibrium atomic and spin dynamics. For each case, 30 independent runs are performed in order to obtain a stable average thermal conductivity. The correlation time considered in our simulations is 16 ps, which is long enough to obtain a converged and steady thermal conductivity (**Figure 2**). An $8 \times 8 \times 8$ unit cell box is used in all EMD simulations, for which size effects may be ignored (**Appendix B**). Lattice expansion due to temperature and spin is considered in our results (**Appendix C**).

For the magnon thermal conductivity computations, 30 independent runs were used to obtain a converged thermal conductivity. A domain of $8 \times 8 \times 8$ unit cells was used, and the correlation time was 16 ps, which is long enough to obtain a converged and size-independent magnon thermal conductivity (**Figure 2** and **Appendix B**).

III. THEORY

A. Thermal Conductivity based on Heat Flux Fluctuation

The energy E of magnetic crystals must account for terms coupling the magnetic spins (E_{spin}) to the lattice ($E_{kinetic}$ and $E_{potential}$) through the following expression [22]:

$$E = E_{kinetic} + E_{potential} + E_{spin} \\ = \sum_{i=1}^N \frac{|\vec{p}|^2}{2m_i} + \sum_{i,j=1}^N V(\vec{r}_{ij}) - \sum_{i,j,i \neq j}^N J(|\vec{r}_{ij}|) \vec{s}_i \cdot \vec{s}_j \quad (4)$$

in which \vec{r} , \vec{p} and \vec{s} are the position, momentum and spin vectors of the atoms, respectively. The negative sign on the last term indicates that the ground state energy of the system considering spin becomes lower. $J(|\vec{r}_{ij}|)$ is the magnetic coupling exchange constant, which originates from two main contributions: (i) direct ferromagnetic exchange between the orbitals localized on centers of ions i and j , and (ii) spin and charge polarizations effects brought by nonmagnetic orbitals. Phonons and magnons are coupled in Eq. (4) via the atomistic positions, i.e., \vec{r}_{ij} . The heat flux due to lattice vibrations takes the form [28]

$$Q_{lattice}''^x = \frac{1}{V} \sum_i \frac{d(E_i^{kinetic} + E_i^{potential}) r_i^x}{dt} \\ = \frac{1}{V} \left\{ \sum_i e_i \cdot v_i^x + \frac{1}{2} \sum_{i=1} \sum_{j=1; j \neq i} (\vec{F}_{ij} \cdot \vec{v}_i) \cdot r_{ij}^x \right\} \quad (5)$$

where e_i and \vec{v}_i are the energy and the velocity of atom i , respectively. \vec{F}_{ij} represents the force between two atoms, V and S are the volume and the cross section area of the system, respectively. and the heat flux associated with spin is expressed as

$$Q_{spin,ij}'' = \frac{1}{S} \frac{dE_{ij}^{spin}}{dt} \\ = \frac{1}{S} J(|\vec{r}_{ij}|) \left(\vec{s}_i \cdot \frac{d\vec{s}_j}{dt} + \vec{s}_j \cdot \frac{d\vec{s}_i}{dt} \right) + \\ \frac{1}{S} \frac{dJ(|\vec{r}_{ij}|)}{dt} \vec{s}_i \cdot \vec{s}_j \quad (6)$$

where \vec{r}_{ij} is the distance between atoms i and j :

$$\vec{r}_{ij} = \vec{r}_i - \vec{r}_j \\ = [\vec{r}_i^0 + \vec{u}_i(t)] - [\vec{r}_j^0 + \vec{u}_j(t)] \\ = \vec{r}_{ij}^0 + \vec{u}_{ij}(t) \quad (7)$$

in which, \vec{r}^0 and \vec{u} are the equilibrium position and displacement of atoms, respectively. Since $|\vec{r}_{ij}^0| \gg |\vec{u}_{ij}|$ (**Appendix D**, we assume that \vec{r}_{ij} is time indepen-

dent. Therefore, Eq. (7) can be rewritten in the form

$$Q_{spin,ij}'' = \frac{1}{S} \frac{dE_{ij}^{spin}}{dt} \\ \approx \frac{J(|\vec{r}_{ij}|)}{S} \left(\vec{s}_i \cdot \frac{d\vec{s}_j}{dt} + \vec{s}_j \cdot \frac{d\vec{s}_i}{dt} \right) \quad (8)$$

At the same time, if we assume the atom i and j are separated by an imaginary interface, the heat flux across the interface can be expressed as

$$Q_{spin}'' = \frac{1}{2S} \sum_{i \in L} \sum_{i \in R} Q_{spin,ij}'' \\ = \frac{1}{2S} \sum_{i \in L} \sum_{i \in R} J(|\vec{r}_{ij}|) \left(\vec{s}_i \cdot \frac{d\vec{s}_j}{dt} + \vec{s}_j \cdot \frac{d\vec{s}_i}{dt} \right) \\ = \frac{1}{S} \sum_{i \in L} \sum_{i \in R} J(|\vec{r}_{ij}|) \frac{d\vec{s}_j}{dt} \cdot \vec{s}_i \quad (9)$$

where L and R indicate left and right sides of the imaginary interface, respectively. The factor $1/2$ considers the ergodicity of the system. In addition, for SLD systems,

$$\frac{d\vec{s}_i}{dt} = \vec{f}_i \times \vec{s}_i = -\frac{1}{\hbar} \frac{\partial E_{mag}}{\partial \vec{s}_i} \times \vec{s}_i \quad (10)$$

in which \vec{f}_i is the analog of a force applied on the spin. Finally, the heat flux across the imaginary interface may be written as

$$Q_{spin}''^x = -\frac{1}{S\hbar} \sum_{i \in L} \sum_{i \in R} J(|\vec{r}_{ij}|) \left(\frac{\partial E_{mag}}{\partial \vec{s}_j} \times \vec{s}_j \right) \cdot \vec{s}_i \quad (11)$$

Based on linear response theory [21] and Eq. (4)-(5), the thermal conductivity of a magnetic system can be divided into contributions from lattice vibrations, κ_{phonon} , spin-related fluctuations, κ_{magnon} , and a term resulting from lattice-spin interactions, κ_{cross} :

$$\kappa = \kappa_{phonon} + \kappa_{magnon} + \kappa_{cross} \\ = \frac{V}{k_b T^2} \int \left[\underbrace{\langle Q_{lattice}''^x(t) \cdot Q_{lattice}''^x(0) \rangle}_{phonon} \right. \\ \left. + \underbrace{\langle Q_{spin}''^x(t) \cdot Q_{spin}''^x(0) \rangle}_{magnon} + 2 \underbrace{\langle Q_{spin}''^x(t) \cdot Q_{lattice}''^x(0) \rangle}_{cross} \right] dt \quad (12)$$

where k_b is the Boltzmann constant, and T is the temperature of the system. We note that κ_{cross} is not the result of phonon-magnon scattering, but of the cross-correlation between the phonon and magnon heat fluxes. Physically, the cross term represented the interaction between the heat carried by the phonons and the heat carried by the magnons that can alter pure phonon and spin heat flow. The effect of magnon scattering on phonon transport is elucidated by calculating the phonon thermal conductivity using ($E = E_{kinetic} + E_{potential} + E_{spin}$) and ($E = E_{kinetic} + E_{potential}$) and comparing the two

values. Similarly, the influence of phonon scattering on magnon thermal conductivity is assessed by computing the magnon thermal conductivity using ($E = E_{kinetic} + E_{potential} + E_{spin}$) and ($E = E_{spin}$) and comparing the two values.

B. Spectral Energy Density

The atomistic velocity and spin change frequency used for the spectral energy density (SED) calculations were output every 4 fs over a total sampling time of 80 ps. All the reduced results were averaged across 3 runs and using two time intervals, i.e., the 80 ps sampling time is divided into two 40 ps intervals. A Gauss window of 0.1 THz is used to filter the noise in the original data. The eigenvectors and frequencies used in our simulations are computed by solving the phonon dynamical matrix equation

$$\omega(\vec{q}, \nu) \vec{e}(\vec{q}, \nu) = \omega(\vec{q}, \nu) D(\vec{q}) \quad (13)$$

and the magnon dynamical matrix equation

$$\omega(\vec{k}) \vec{e}(\vec{k}) = D(\vec{k}) \vec{e}(\vec{k}) \quad (14)$$

where $D(\vec{q})$ and $D(\vec{k})$ are the lattice and spin dynamical matrices and have the form

$$D(\vec{q}) = \frac{1}{m} \sum_l K(0, l) \exp(i\vec{k}[\vec{r}(l) - \vec{r}(0)]) \quad (15)$$

and

$$D(\vec{k}) = \frac{1}{\hbar} \sum_l J(0, l) \cdot [1 - \exp(i\vec{k}[\vec{r}(l) - \vec{r}(0)])] \quad (16)$$

respectively. Here, K is the force constant matrix. We note that Eq. (16) is derived assuming the material is ferromagnetic, in which all the spins have the same magnitude in one direction (only under this assumption can the spin motion equation can be reduced to Eq. (14) [29]). The volumetric heat capacity and group velocity of phonons and magnons are shown in **Appendix E**. Together with the Boltzmann transport equation (BTE), the thermal conductivity can be obtained.

IV. RESULTS

A. The Total Thermal Conductivity

From Eqs. (4) and (5), the net heat flux of lattice vibrations ($Q''_{lattice}$) and spin fluctuations (Q''_{spin}) in EMD simulations should be zero, which is validated by our numerical results (**Figure 2a** and **1b**). Furthermore, following linear response theory, the thermal conductivity of the two heat carriers should converge with the increasing correlation time [Eq. (4)], and this is also reflected in our simulations (**Figure 2c**).

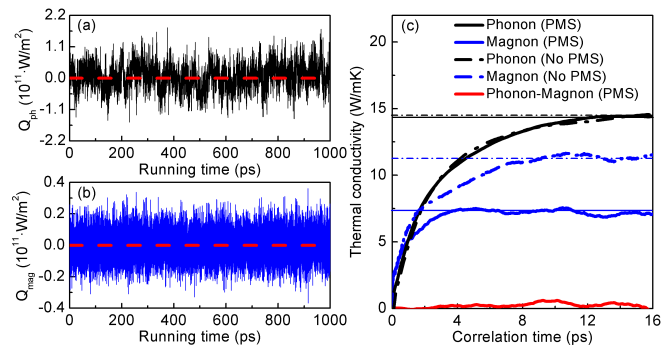


FIG. 2: (a) Heat flux of phonons and (b) magnons. (c) Thermal conductivity of phonons and magnons calculated using GKEASD at 300 K. Computations are performed with and without phonon-magnon scattering (PMS).

To evaluate thermal conductivity behavior at different temperatures, the order of the spin configuration in our system is calculated via

$$P_{order} = \sqrt{\frac{\sum_{\alpha=x,y,z} \left(\sum_i s_{i,\alpha}^T \right)^2}{\sum_{\alpha=x,y,z} \left(\sum_i s_{i,\alpha}^{T=0} \right)^2}} \quad (17)$$

where $P_{order} = 1$ in the ferromagnetic limit and $P_{order} = 0$ in the paramagnetic limit. Small values of P_{order} indicate that spins in the system are predominantly disordered, which leads to broken periodicity.

By considering the contributions of both phonons and magnons (**Appendix F**), the predicted total thermal conductivity is in broad agreement with experimental measurements [6, 7] over the temperature range from 300 K to 1200 K (**Figure 3a**) (the electrical thermal conductivity was subtracted from the experimental measurements). We note that the two experimental results [6, 7] in **Figure 3a** are themselves quite different from each other, and the disagreement between them is larger than that caused by phonon-magnon scattering in the simulations. Thus, they cannot definitively establish the accuracy of our phonon-magnon scattering models. A number of reasons may account for these differences: (i) loss of heat from the specimen due to conduction through leads; (ii) impurities in the sample, which in Ref. [6] may be as high as 1%.

An important feature in **Figure 3a** is the sharp fall in thermal conductivity reported in the experimental data of Ref. [7] near the Curie temperature (around 1200 K) due to the ferromagnetic-to-paramagnetic transition. Previously published atomic spin dynamics or spin lattice dynamics simulations have been known to smooth the ferromagnetic-to-paramagnetic phase transition near the Curie temperature [30, 31] (see P_{order} with original J in **Figure 3a**). One explanation is that the simulation of atomic spins is performed within a classical framework and ignores quantum effects [31, 32]. However, as discussed below and well established in Ref. [32], quantum effects can be ignored for phonon and magnon thermal transport properties in the temperature range considered here. Another explanation for the transition is that the value of the magnetic exchange parameter J

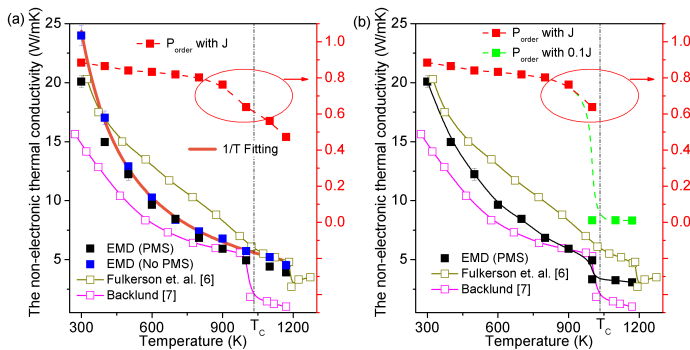


FIG. 3: (a) Adjusted total thermal conductivity for invariant magnetic exchange coefficient J , and (b) adjusted total thermal conductivity with temperature dependent magnetic exchange constant. The EMD results are averaged over 30 independent runs. The experimental results are the so called “lattice thermal conductivities” in Ref. [6, 7]. Here, the transition temperature for J is assumed to be 1000 K rather than the Curie temperature of 1200 K in order to better match experimental data.

varies as a function of temperature [30, 33].

Our EMD simulations (black and blue symbols) in **Figure 3a** use a single, temperature-invariant value of J and treat the spins as classical, and therefore the results do not exhibit the experimentally observed sharp fall in thermal conductivity. To explore this issue further, an additional set of computations was performed (**Figure 3b**) wherein the value of J varies with temperature. Here, we adjust the J to make sure the spin in the system of paramagnetic state is fully disordered because J is only parameter that determines the spin configuration in the system. We assume that J is constant when $T < T_c$, while J is one tenth of the low temperature value when $T > T_c$ (**Figure 3b**), indicating that the spin configuration in the system is fully disordered (i.e., the paramagnetic limit). Consequently, the non-electronic thermal conductivity drops sharply around the Curie temperature due to the decrease in magnon thermal conductivity (**Appendix G**), consistent with the experimental observations [6, 7].

At the same time, phonon-magnon scattering does not exhibit a strong effect on thermal transport in BCC iron because the values of both the phonon and the magnon thermal conductivities are relatively small, i.e., phonon-phonon scattering and magnon-magnon scattering are the dominant scattering mechanisms in such materials.

B. Phonon-magnon Scattering Process

To further understand the temperature behavior of thermal conductivity, mode-level phonon and magnon scattering rates have been calculated at three temperatures, 300 K, 700 K and 1100 K, by SED analysis (**Appendix H**):

$$|\Phi|^2 = \frac{I_p}{[(\omega - \omega_p)/\Delta]^2 + 1} \quad (18)$$

where I_p and ω_p are the peak magnitude and frequency at the peak center, respectively. Δ is the linewidth, which is half of the scattering rate Γ . Φ is the spectral energy, which takes the following form for phonons [34, 35]:

$$\Phi(\vec{q}, \nu) \sim \frac{1}{\sqrt{2\pi t_0}} \int_0^{t_0} \sum_{jl} m_j \exp[i\vec{q} \cdot \vec{r}(jl) - i\omega t] \cdot \vec{e}^*(j, \vec{q}, \nu) \vec{v}(jl, t) dt \quad (19)$$

and, for magnons, can be written as [36]:

$$\Phi(\vec{k}, \mu) \sim \frac{\hbar}{\sqrt{2\pi t_0}} \int_0^{t_0} \sum_{jl} \exp[i\vec{k} \cdot \vec{r}(jl) - i\omega t] \cdot \vec{e}^*(j, \vec{k}, \mu) \frac{d\vec{s}(jl, t)}{dt} dt \quad (20)$$

where \vec{e} is the mode eigenvector of a phonon or magnon, and t_0 is the integration limit. Using Matthiessen’s rule, phonon-magnon ($\Gamma_{\text{phonon-magnon}}$, in units of $1/ps$) and magnon-phonon ($\Gamma_{\text{magnon-phonon}}$) scattering rates can be calculated via:

$$\Gamma_{\text{phonon-magnon}} = \Gamma_{\text{phonon}}^{\text{magnon}} - \Gamma_{\text{phonon}}^{\text{no magnon}} \quad (21)$$

$$\Gamma_{\text{magnon-phonon}} = \Gamma_{\text{magnon}}^{\text{phonon}} - \Gamma_{\text{magnon}}^{\text{no phonon}} \quad (22)$$

where the superscripts *magnon* and *no magnon* indicate that the lattice vibrates with and without spins in the system, respectively, and vice versa for *phonon* and *no phonon* (**Appendix H**).

From the phonon-magnon scattering results (**Figure 3a**), we observe a general tendency that high-frequency phonons (ω larger than 4.3 THz) are scattered by magnons more strongly than low-frequency phonons because the magnon energy is much larger than the phonon energy (**Figure 3c**). For phonon-dominant magnetic materials in which the thermal conductivity is mainly due to phonons, magnons may scatter phonons [37, 38] through phonon emission or absorption, $\hbar\omega(\vec{k}', \mu') = \hbar\omega(\vec{q}, \nu) + \hbar\omega(\vec{k}, \mu)$. Referring to **Figure 3c**, and considering a magnon of energy $\hbar\omega_A$ scattered by a magnon of energy $\hbar\omega_B$, a high-frequency phonon would have a greater probability of involvement in a phonon-magnon scattering process than a low-frequency phonon. For instance, only two channels exist for the magnon $\hbar\omega_A$ to be scattered to the magnon $\hbar\omega_B$ when the phonon energy is $\hbar\omega = 12.41$ meV ($\omega = 3$ THz), whereas the number of channels for the magnon $\hbar\omega_A$ to be scattered to the magnon $\hbar\omega_C$ is four when the phonon energy is 37.6 meV ($\omega = 9.1$ THz, the highest phonon frequency). From the magnon dispersion curve, the frequency changes for the small (P1-P2) and large peaks (P2-P3) are 4.3 and 3.6 THz, respectively; therefore, phonons (magnons) above 4.3 (68) THz have a much greater chance to be involved in phonon-magnon scattering processes.

Another reason that high-frequency phonons are preferentially involved in phonon-magnon scattering processes is the high density of states of phonons in the high-

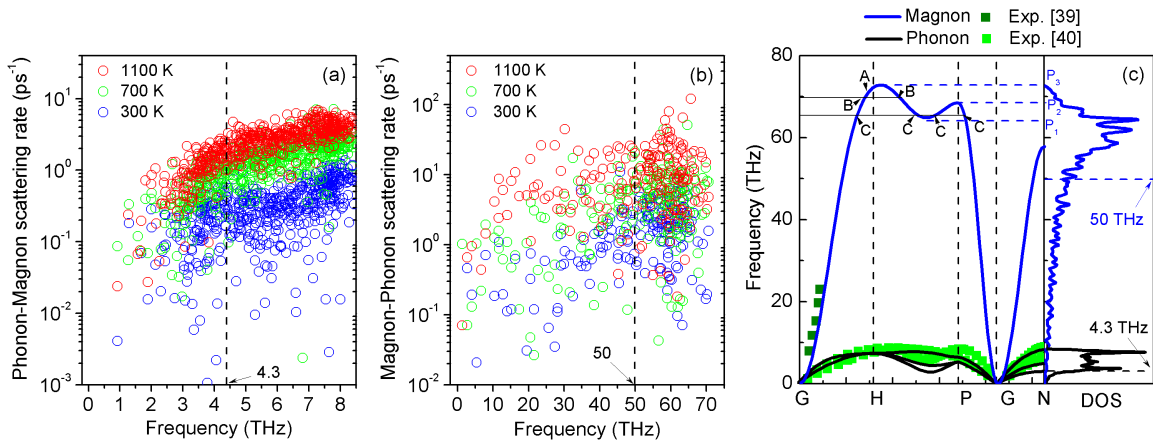


FIG. 4: (a) Computed phonon-magnon and (d) magnon-phonon scattering rates based on Matthiessen's rule. (c) Phonon and magnon dispersions. Experimental data is from Ref. [39, 40]

frequency region (**Figure 3c**). First-principles calculations [15] and experimental measurements [41] also confirm that high-frequency phonons are more strongly scattered by magnons. For materials in which the magnon thermal conductivity is dominant, magnons are scattered by phonons [37, 38] via phonon absorption or emission processes $\hbar\omega(\vec{k}', \mu') \pm \hbar\omega(\vec{q}, \nu) = \hbar\omega(\vec{k}, \mu)$. The magnon-phonon scattering rate of high-frequency magnons is somewhat higher than that of low-frequency magnons (**Figure 3b**) because high-frequency magnons have a larger density of states (**Figure 3c**). The phenomena discussed above become more apparent at increased temperatures, which strengthen the scattering among the heat carriers.

C. The Accumulative Thermal Conductivity

To facilitate the analysis of thermal conductivity contributions, the thermal conductivity accumulation function has been computed with respect to the mean free path Λ using

$$\kappa(\Lambda) = \sum_{\Lambda < \Lambda_0} c_v v_g \Lambda = \sum_{\Lambda < \Lambda_0} c_v v_g^2 \tau \quad (23)$$

where c_v , v_g (**Appendix E**) and τ are the volumetric heat capacity, group velocity, and relaxation times of phonons and magnons, respectively. For phonons (**Figure 4a**), at $T = 300$ K, the accumulated thermal conductivities with and without spin are similar, indicating that magnons do not have a strong effect on phonon thermal conductivity near room temperature. This is due to the fact that long mean free path phonons are the main contributors to thermal conductivity, and these phonons do not easily scatter with magnons, as discussed above. However, at 700 K, the phonon mean free path falls to 0.3 - 4 nm, which is much smaller than that at 300 K due to strong phonon-phonon scattering (black triangle symbols in **Figure 4a**). Furthermore, high-frequency phonons with short mean free paths (0.4 - 0.8 nm) are more easily scattered by magnons. Consequently, the total lattice thermal con-

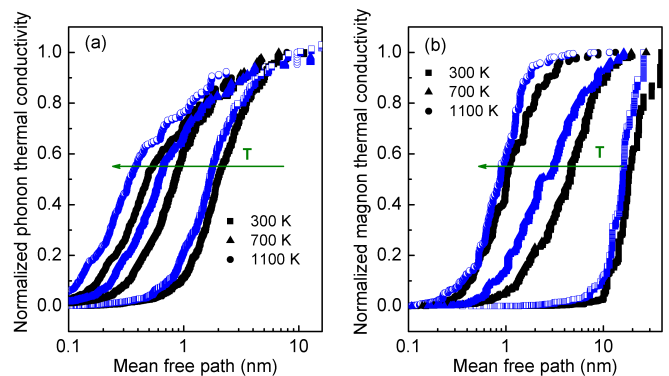


FIG. 5: (a) Thermal conductivity accumulation function of phonons and (b) magnons at various temperatures. The black and blue dots represent results (a) without and with spin, and (b) without and with phonons, respectively.

ductivity of magnetic BCC iron becomes slightly smaller than that of non-magnetic BCC iron (**Appendix H**). Finally, at 1100 K phonons are scattered strongly by both phonons and magnons because high temperatures increase the vibration magnitude of lattice and spin excitations. For magnons (**Figure 4b**) at room temperature, only the long-mean-free-path, or equivalently, low-frequency magnons are scattered by phonons because only these magnons transport significant energy, i.e., the heat capacity of high frequency magnons is very small (**Appendix E**). When the system temperature increases to 700 K and then to 1100 K, the mean free path of magnons becomes much shorter than that at 300K, and the short mean free path (high frequency) magnons are scattered by phonons strongly.

V. DISCUSSIONS

We also note that the magnon group velocities are calculated here from the magnon dispersion without considering temperature effects, i.e., assuming a ferromagnetic system. Such an assumption may introduce inaccuracies in the magnon mean free path and modal thermal conductivity computations. At 300 K, the total magnon

thermal conductivity calculated using BTE, i.e., using $\kappa = \sum c_v v_g^2 \tau$ with the values of relaxation time computed using SED, is 10.1 W/mK. This value is lower than the BTE results of Wu *et. al.* (15.2 W/mK) due to their overestimation of the magnon dispersion [36], whereas it is 7.8 W/mK computed by GK-ESAD. The closer correspondence between BTE and GKEASD at room temperature indicates that the system may be treated as ferromagnetic at 300 K. However, the total magnon thermal conductivities calculated by BTE (GKEASD) are 11.1 (1.9) and 56.9 (1.2) W/mK at 700 K and 1100 K, respectively. The large differences between SED-BTE and GKEASD indicate that the magnon group velocity is overestimated, and the calculation should consider spin disorder at high temperatures.

Before concluding our study, we briefly highlight two limitations that our methodology inherited from the SLD formalism. In our calculations, the exchange integral J_{ij} is assumed to remain constant, and its dependence on temperature is neglected. Recent studies have investigated this dependence and proposed methodologies to account for it [31, 33]. Encapsulating them within our framework could improve the accuracy of predictions. Furthermore, the simulation of classical spins (instead of quantum spins) is known to make the ferromagnetic to paramagnetic phase transition smoother than in the experimental observations. Implementing quantum baths and statistics has proven possible to reproduce more accurately the sharp transition occurring at T_c [30, 31]. However, as the GK-ESAD framework is based on equilibrium molecular dynamics, the associated simulations do not involve a connection to a random bath. Overall, an empirical parametrization of the exchange integral J_{ij} could account for both its temperature dependence and the sharp transition occurring at T_c .

VI. CONCLUSIONS

In conclusion, we have developed a temperature-dependent method, the Green-Kubo equilibrium atomic and spin dynamics method, to calculate coupled phonon and magnon transport in magnetic materials. Reasonably good agreement is obtained between our simulation results and experimental measurements in computing dispersion curves and temperature dependent thermal conductivity, and these results suggests that the approach captures the overall heat transfer behavior of phonons and magnons in magnetic crystals. Analysis of scattering processes between phonons and magnons indicate that high-frequency phonon scattering rates due to phonon-magnon scattering are much larger than those at low frequencies because of energy-conserving rules for scattering and the high density of states. The application of this new methodology will yield deeper insights into the thermal transport properties of other phonon- or magnon-dominant materials.

ACKNOWLEDGMENTS

This work was supported by the Nation Science Foundation (NSF) (Project number: NSF1758004) and used computational and storage services associated with the Hoffman2 Shared Cluster provided by UCLA Institute for Digital Research and Educations Research Technology Group. Y. Z. gratefully acknowledges Dr. Zheyong Fan (Aalto University) for valuable comments and proof reading the manuscript. J. T. acknowledges that Sandia National Laboratories is a multi-mission laboratory managed and operated by National Technology and Engineering Solutions of Sandia, LLC, a wholly owned subsidiary of Honeywell International Inc., for the U.S. Department of Energy's National Nuclear Security Administration under contract DE-NA0003525. This paper describes objective technical results and analysis. Any subjective views or opinions that might be expressed in the paper do not necessarily represent the views of the U.S. Department of Energy or the United States Government.

APPENDIX

A. Phonon Dispersions

To assess the accuracy of the potential, we compare the phonon dispersion (**Figure 2**) from MD and *ab initio* calculations, and good agreement is found.

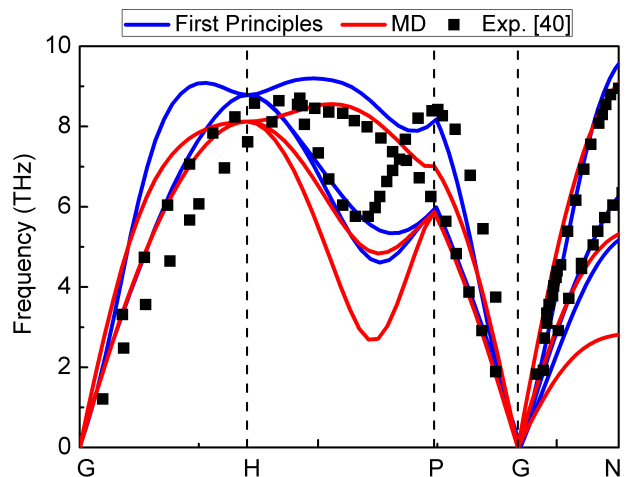


FIG. 6: Phonon dispersion from MD and first principles calculations. The black dots are experimental values [40].

B. Converge Test

For phonons, an $8 \times 8 \times 8$ unit cell box is used in all EMD simulations, for which size effects may be ignored (**Figure 4**). For magnons, a domain of $8 \times 8 \times 8$ unit cells was used, and the correlation time was 16 ps, which is long enough to obtain a converged and size-independent magnon thermal conductivity.

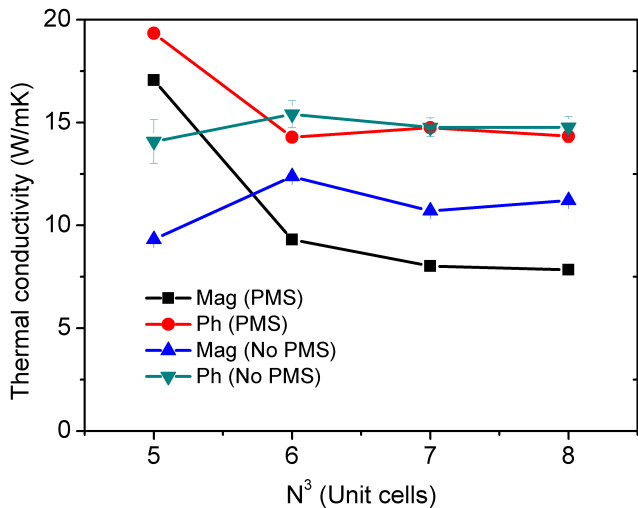


FIG. 7: Convergence test for GK-ESAD. PMS indicates the presence of phonon-magnon scattering. N is the number of unit cell along one direction.

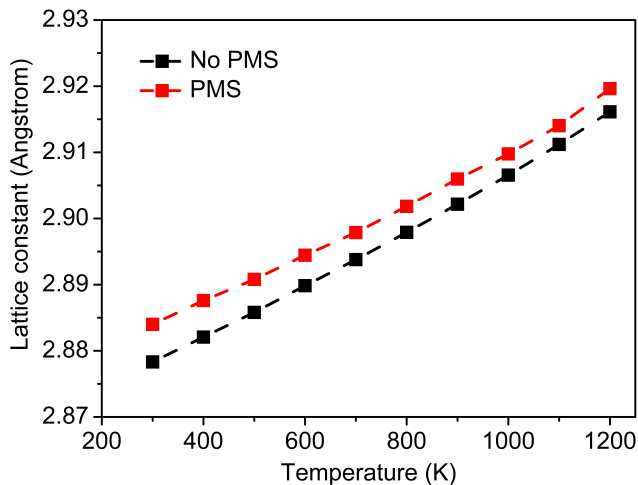


FIG. 8: Lattice constant vs. temperature with and without considering spin effects.

C. Lattice Expansion

Lattice expansion due to temperature and spin is considered in our results.

D. Displacement between Atoms

The relative displacement between atom i and j (Figure 3).

E. Heat Capacity and Group Velocity

The volumetric heat capacity and group velocity of phonons and magnons are shown in Figure 8. Together with the Boltzmann transport equation (BTE), the thermal conductivity can be obtained.

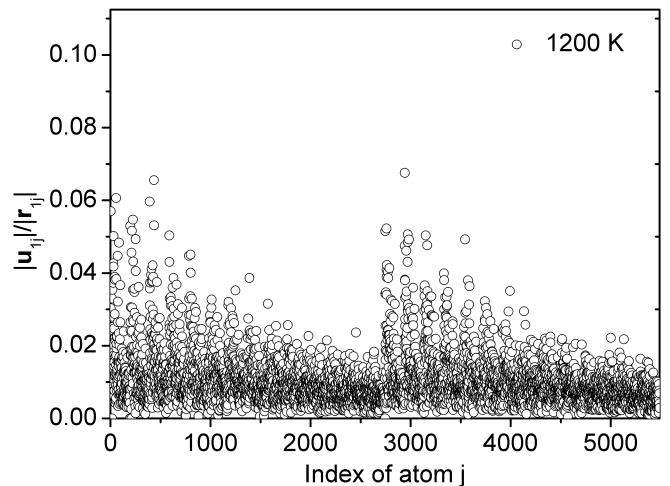


FIG. 9: Relative displacement between atom i and j .

F. Thermal Conductivity of Phonons and Magnons

The temperature-dependent lattice thermal conductivity of BCC iron with and without the influence of spins is plotted in Figure 11a. Magnons affect the lattice thermal conductivity of magnetic BCC iron most prominently at the high temperatures, i.e., above 800 K where the phonon-magnon scattering is strong enough to affect the phonon thermal conductivity.

Furthermore, in order to evaluate quantum effects in MD simulations that may affect phonon thermal conductivity, the thermal conductivity of nonmagnetic BCC Fe using the Boltzmann Transport Equation (BTE) with force constant inputs from first principles and classical potentials was also calculated (details are given in Appendix I). Our results show that approximating the Bose-Einstein distribution by the Boltzmann distribution has a negligible effect on phonon thermal conductivity (Figure 11a). Meanwhile, first-principles calculations (Figure 11a) also indicate that the mechanical potential used in our simulations somewhat overestimates lattice thermal conductivity. However, the deviation is sufficiently small that it is not expected to change the main conclusions.

G. Magnetic Exchange Parameter Dependent Thermal Conductivity

Figure 12 shows the thermal conductivity with a temperature-dependent magnetic exchange parameter J . In Figure 12, we assume J is a constant when $T \leq T_c$, while J is one tenth of the low temperature value when $T \geq T_c$. Using such a strategy, the disorder parameter drops to zero beyond the Curie temperature, which will lead to large decrease of magnon thermal conductivity. Consequently, the total thermal conductivity exhibits a large drop around the Curie temperature.

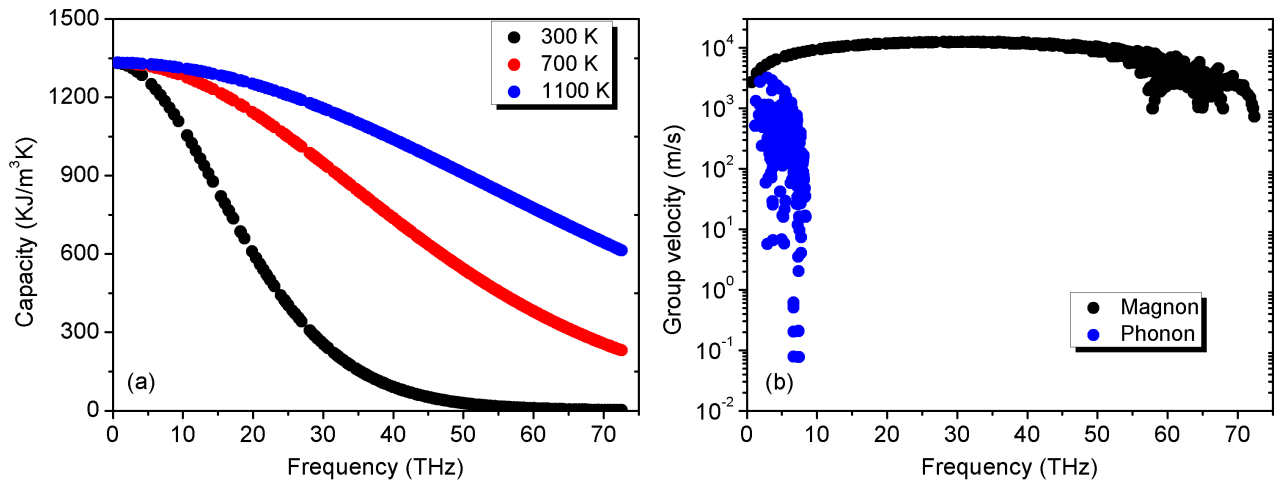


FIG. 10: (a) Volumetric heat capacity and (b) group velocity of phonons and magnons.

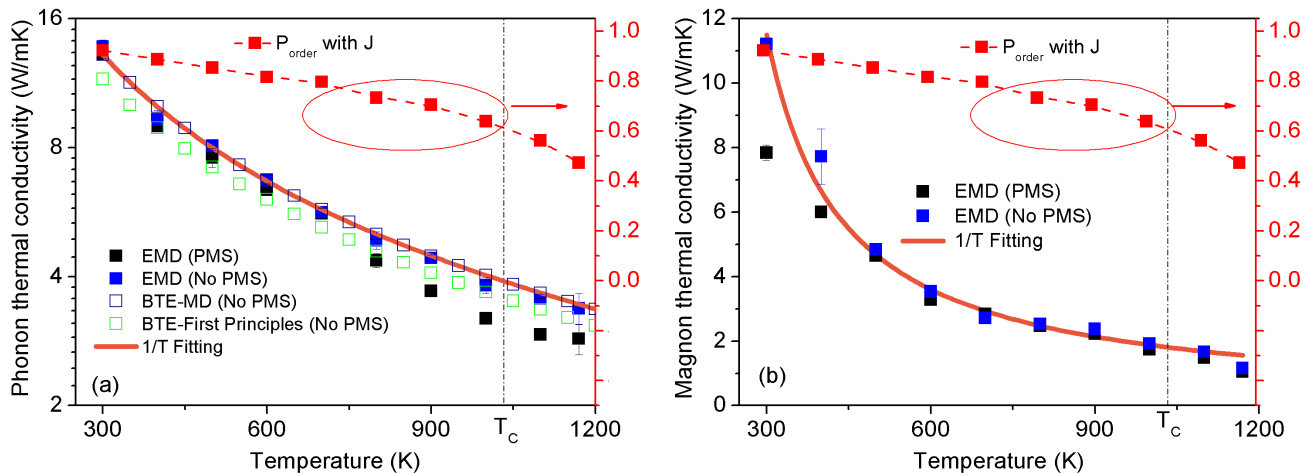


FIG. 11: (a) Thermal conductivity of phonons and (b) magnons with and without PMS (phonon-magnon scattering).

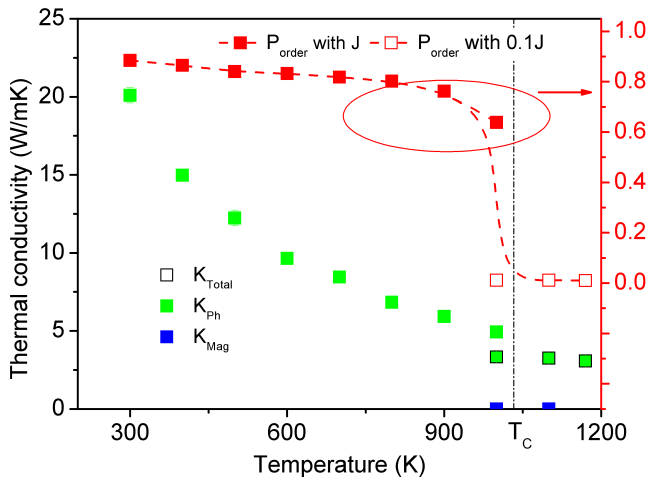


FIG. 12: Relative displacement between atom i and j .

H. Phonon and Magnon Relaxation Time

For comparison, the phonon (magnon) scattering rate of the same system without considering the effects of magnons (phonons) was also calculated based on SED. For the phonons, our results show that (Figure 13a) the scattering rate in the low-frequency region changes

little with the introduction of spin. Low-frequency phonons are known to be the main contributors to thermal conductivity at low temperatures whereas high-frequency phonons (i.e., short mean free path phonons) are important for lattice thermal conductivity at high temperatures [42]. The explanations here provide the reason why the lattice thermal conductivity considering spin is similar to that without it at low temperature (see Figure 11a).

For magnons (Figure 13b), the scattering rates for the system with and without lattice vibrations are similar in this regime (below 50 THz), which indicates that the influence of phonon-magnon scattering on magnon transport in the low frequency region is not important. On the other hand, in the high frequency regime (above 50 THz), magnons can be strongly scattered by phonons.

I. Boltzmann Transport Equation

The BTE can be solved by expanding the scattering term into its first-order perturbation f . Without considering impurities and boundaries, the linearized BTE

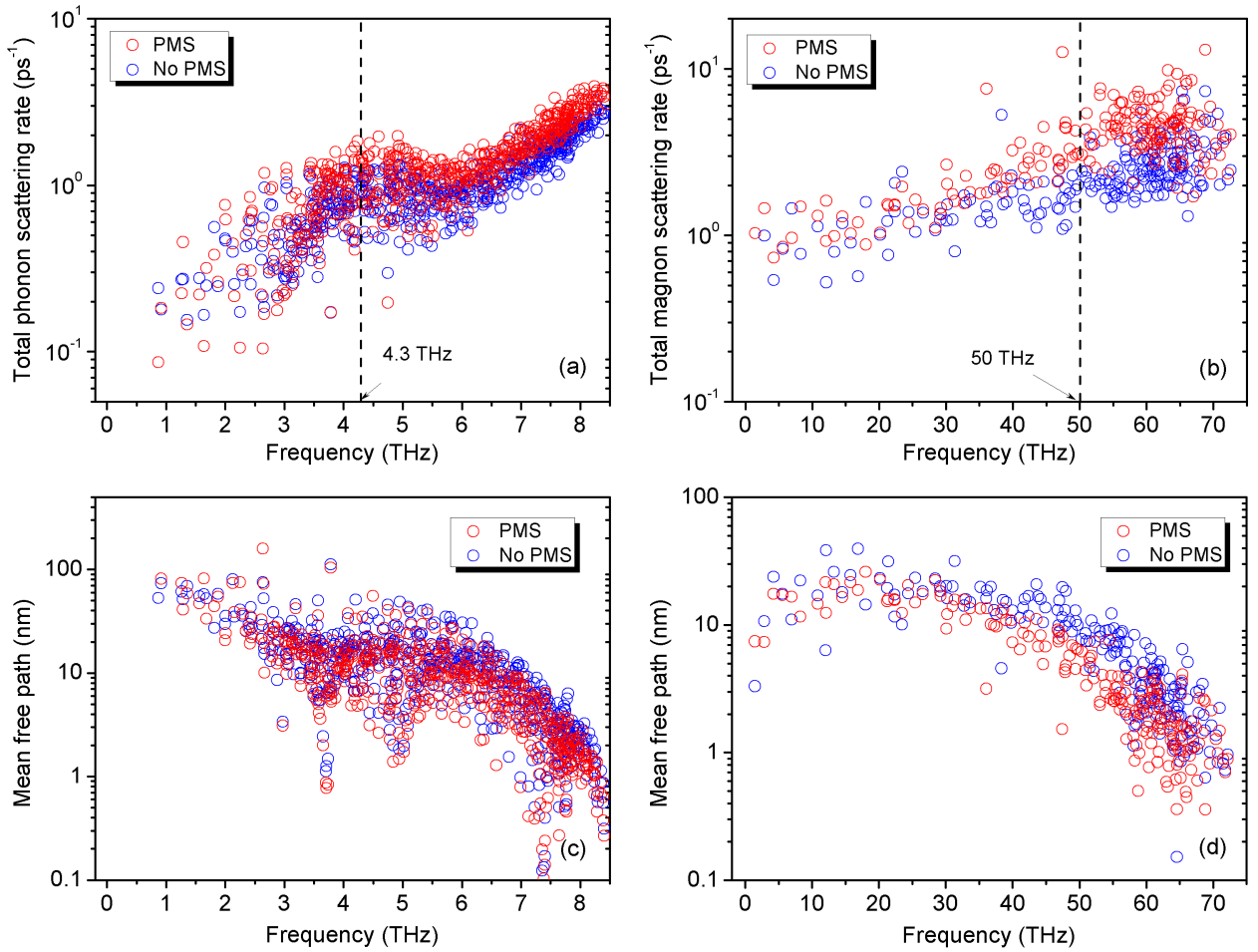


FIG. 13: (a) Phonon and (b) magnon scattering rate with and without considering phonon-magnon scattering at 300 K. The corresponding (c) phonon and (d) magnon mean free paths.

may be recast as [43]

$$\begin{aligned}
 -c(\vec{q}, \nu) \left(\frac{\partial \bar{n}(\vec{q}, \nu)}{\partial T} \right) = & \\
 \sum_{(\vec{q}', \nu'), (\vec{q}'', \nu'')} & \left[\Gamma_{(\vec{q}, \nu), (\vec{q}', \nu'), (\vec{q}'', \nu'')}^{(\vec{q}, \nu)} (f_{(\vec{q}, \nu)}^1 + f_{(\vec{q}', \nu')}^1 - f_{(\vec{q}'', \nu'')}^1) + \right. \\
 & \left. \frac{1}{2} \Gamma_{(\vec{q}, \nu), (\vec{q}'', \nu'')}^{(\vec{q}', \nu')} (f_{(\vec{q}, \nu)}^1 - f_{(\vec{q}', \nu')}^1 - f_{(\vec{q}'', \nu'')}^1) \right] \quad (24)
 \end{aligned}$$

where (\vec{q}, ν) is the phonon mode with wave vector \vec{q} and branch ν . c , \bar{n} and T are the specific heat capacity, equilibrium phonon population and system temperature, respectively. Γ is the scattering rate at equilibrium of a process where two phonons combine to generate a third phonon or when one phonon splits into two phonons. The scattering rate matrix can be obtained using Fermi's Golden Rule. The lattice thermal conductivity may be found by computing the heat flux from the computed phonon distribution and using Fourier's law. The mesh density used in the BTE is $17 \times 17 \times 17$, and a 5^{th} neighbor cutoff is used to compute the 3^{rd} order force constant. A convergence test for the BTE appears in **Figure 14**.

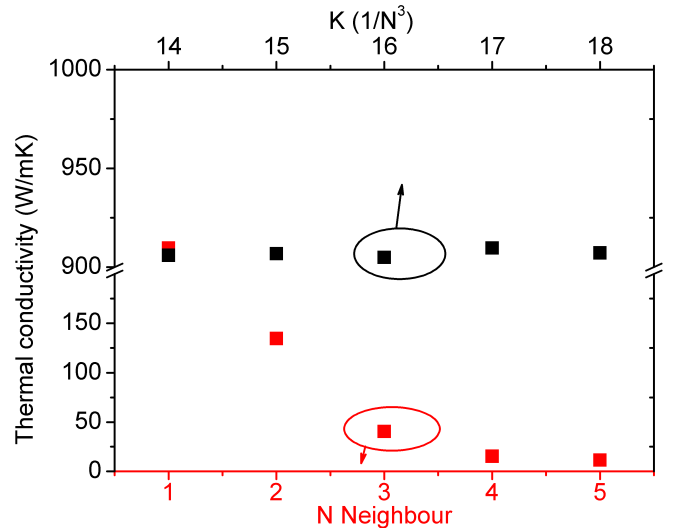


FIG. 14: Convergence test for BTE calculations. N is the number of the neighbour.

* Electronic address: jtranch@sandia.gov

† Electronic address: jmurthy@ucla.edu

‡ Electronic address: tsfisher@ucla.edu

[1] K. Uchida, T. Nonaka, T. Ota and E. Saitoh, Appl.

- Phys. Lett. **97**, 262504 (2010).
- [2] J. Flipse, F. L. Bakker, A. Slachter, F. K. Dejene and B. J. Van Wees, *Nature Nanotech.* **7**, 166 (2012).
- [3] K. Uchida, H. Adachi, T. An, T. Ota, M. Toda, B. Hillebrands, S. Maekawa and E. Saitoh, *Nature Mater.* **10**, 737 (2011).
- [4] G. E. Bauer, E. Saitoh and B. J. Van Wees, *Nature Mater.* **11**, 391 (2012).
- [5] G. Chen and W. A. Goddard, *Science* **239**, 899 (1988).
- [6] W. Fulkerson, J. P. Moore and D. L. McElroy, *J. Appl. Phys.* **37**, 2639 (1966).
- [7] N. G. Bäcklund, *J. Phys. Chem. Solids* **20**, 1 (1961).
- [8] R. W. Powell, R. P. Tye and M. J. Hickman, *Int. J. Heat Mass Tran.* **8**, 679 (1965).
- [9] P. A. Sharma, J. S. Ahn, N. Hur, S. Park, S. B. Kim, S. Lee, J. Park, S. Guha and S. W. Cheong, *Phys. Rev. Lett.* **93**, 177202 (2004).
- [10] P. Tome, D. Logvinovich, J. Hejtmek, M. H. Aguirre and A. Weidenkaff, *Acta Mater.* **59**, 1134 (2011).
- [11] O. Jankovský, D. Sedmidubský, S. Huber, P. Simek and Z. Sofer, *J. Eur. Ceram. Soc.* **34**, 4131 (2014).
- [12] M. G. Holland, *Phys. Rev.* **132**, 2461 (1963).
- [13] J. Callaway, *Phys. Rev.* **113**, 1046 (1959).
- [14] Y. Zhou, Z. Fan, G. Qin, J. Yang, T. Ouyang and M. Hu, *ACS Omega* **3**, 3278 (2018).
- [15] F. Körmann, B. Grabowski, B. Dutta, T. Hickel, L. Mauger, B. Fultz and J. Neugebauer, *Phys. Rev. Lett.* **113**, 165503 (2014).
- [16] I. Stockem, A. Bergman, A. Glensk, T. Hickel, F. Körmann, B. Grabowski, J. Neugebauer and B. Alling, *arXiv:1802.02934* (2018).
- [17] R. F. Sabiryanov and S. S. Jaswal, *Phys. Rev. Lett.* **83**, 2062 (1999).
- [18] B. Liao, J. Zhou and G. Chen, *Phys. Rev. Lett.* **113**, 25902 (2014).
- [19] Y. Liu, L. Xie, Z. Yuan and K. Xia, *Phys. Rev. B* **96**, 174416 (2017).
- [20] A. Dick, B. Grabowski, T. Hickel, J. Neugebauer and F. Körmann, *Phys. Rev. B* **85**, 125104 (2012).
- [21] R. Kubo, *J. Phys. Soc. Jpn* **12**, 570 (1957).
- [22] J. Tranchida, S. J. Plimpton, P. Thibaudeau and A. P. Thompson, *J. Comp. Phys.* (2018).
- [23] C. X. Quintela, F. Rivadulla and J. Rivas, *Appl. Phys. Lett.* **94**, 152103 (2009).
- [24] S. Plimpton, *J. Comput. Phys.* **117**, 1 (1995).
- [25] M. Pajda, J. Kudrnovsk, I. Turek, V. Drchal and P. Bruno, *Phys. Rev. B* **64**, 174402 (2001).
- [26] H. Chamati, N. I. Papanicolaou, Y. Mishin and D. A. Papaconstantopoulos, *Surf. Sci.* **600**, 1793 (2006).
- [27] J. P. Perdew, *Phys. Rev. B* **33**, 8822 (1986).
- [28] R. J. Hardy, *Phys. Rev.* **132**, 168 (1963).
- [29] C. Kittel, *Quantum theory of solids* (Wiley, 1987)
- [30] L. Bergqvist and A. Bergman, *Phys. Rev. Mater.* **2**, 013802 (2018)
- [31] A. Szilva, M. Costa, A. Bergman, L. Szunyogh, L. Nordström and O. Eriksson, *Phys. Rev. Lett.* **111**, 127204 (2013).
- [32] J. E. Turney, A. McGaughey and C. H. Amon, *Phys. Rev. B* **79**, 224305 (2009).
- [33] A. Ruban and M. Dehghani, *Phys. Rev. B* **94**, 104111 (2016).
- [34] J. A. Thomas, J. E. Turney, R. M. Iutzi, C. H. Amon and A. J. McGaughey, *Phys. Rev. B* **81**, 81411 (2010).
- [35] Y. Zhou, X. Zhang and M. Hu, *Phys. Rev. B* **92**, 195204 (2015).
- [36] X. Wu, Z. Liu and T. Luo, *J. Appl. Phys.* **123**, 85109 (2018).
- [37] A. L. Chernyshev and W. Brenig, *Phys. Rev. B* **92**, 54409 (2015).
- [38] G. L. Stamokostas, P. E. Lapas and G. A. Fiete, *Phys. Rev. B* **95**, 64410 (2017).
- [39] H. A. Mook and R. M. Nicklow, *Phys. Rev. B* **7**, 336 (1973).
- [40] V. J. Minkiewicz, G. Shirane and R. Nathans, *Phys. Rev.* **162**, 528 (1967).
- [41] L. Mauger, M. S. Lucas, J. A. Muoz, S. J. Tracy, M. Kresch, Y. Xiao, P. Chow and B. Fultz, *Phys. Rev. B* **90**, 064303 (2014).
- [42] J. Cuffe, J. K. Eliason, A. A. Maznev, K. C. Collins, J. A. Johnson, A. Shchepetov, M. Prunnila, J. Ahopelto, C. M. S. Torres and G. Chen, *Phys. Rev. B* **91**, 245423 (2015).
- [43] W. Li, J. Carrete, N. A. Katcho and N. Mingo, *Comput. Phys. Commun.* **185**, 1747 (2014).